nature materials

ARTICLES

PUBLISHED ONLINE: 16 FEBRUARY 2015 | DOI: 10.1038/NMAT4203

# Dysprosium-doped cadmium oxide as a gateway material for mid-infrared plasmonics

Edward Sachet[1], Christopher T. Shelton[1], Joshua S. Harris[1], Benjamin E. Gaddy[1], Douglas L. Irving[1], Stefano Curtarolo[2]*, Brian F. Donovan[3], Patrick E. Hopkins[4], Peter A. Sharma[5], Ana Lima Sharma[5], Jon Ihlefeld[5], Stefan Franzen[6] and Jon-Paul Maria[1]*

**The interest in plasmonic technologies surrounds many emergent optoelectronic applications, such as plasmon lasers, transistors, sensors and information storage. Although plasmonic materials for ultraviolet–visible and near-infrared wavelengths have been found, the mid-infrared range remains a challenge to address: few known systems can achieve subwavelength optical confinement with low loss in this range. With a combination of experiments and *ab initio* modelling, here we demonstrate an extreme peak of electron mobility in Dy-doped CdO that is achieved through accurate 'defect equilibrium engineering'. In so doing, we create a tunable plasmon host that satisfies the criteria for mid-infrared spectrum plasmonics, and overcomes the losses seen in conventional plasmonic materials. In particular, extrinsic doping pins the CdO Fermi level above the conduction band minimum and it increases the formation energy of native oxygen vacancies, thus reducing their populations by several orders of magnitude. The substitutional lattice strain induced by Dy doping is sufficiently small, allowing mobility values around 500 $cm^2 V^{-1} s^{-1}$ for carrier densities above $10^{20}$ $cm^{-3}$. Our work shows that CdO:Dy is a model system for intrinsic and extrinsic manipulation of defects affecting electrical, optical and thermal properties, that oxide conductors are ideal candidates for plasmonic devices and that the defect engineering approach for property optimization is generally applicable to other conducting metal oxides.**

Plasmonic phenomena in the mid-infrared offer an exciting complement to established plasmonic technologies that operate in the ultraviolet–visible to near-infrared energies. High-value-added applications enabled by mid-infrared operation range from targeted chemical sensing, thermography, heat harvesting and heat-assisted magnetic data recording to light emitters such as quantum cascade lasers. Gold and silver are the most common plasmonic conductors. However, they are lossy resonators in the mid-infrared (owing to their high electron concentration and inter-/intraband transitions[1]) and their carrier concentrations cannot be tuned. Consequently, they are not appropriate for this lower-energy spectral range.

The urgency for a low-loss, easy-to-manufacture and abundant material exhibiting high-quality plasmon resonance in the mid-infrared range has been raised with insistence[2–5]. Until now, a solution has not been found. In this work, we present the conductive metal oxide (CMO) dysprosium-doped cadmium oxide (CdO:Dy) as the first gateway material for infrared plasmonics. Although CMOs such as indium tin oxide and aluminium-doped zinc oxide exhibit plasmon resonance in mid-infrared energies and are tunable, their utility is limited by consistently low mobility values. Graphene and patterned graphene structures support various plasmon modes in the mid-infrared[6,7]; however, performance is limited to wavelengths >6.5 μm owing to scattering with optical phonons[8]. Highly doped semiconductors such as n-InAs have been reported to support low-loss plasmons, but doping limits below $1 \times 10^{20}$ $cm^{-3}$ restrict such materials for longer-wavelength applications (>5.4 μm; refs 9,10). While semiconductor metasurfaces that couple to infrared light are of interest for plasmonics, efforts so far are still nascent[11]. We demonstrate in CdO how defect equilibria can be actively manipulated to achieve a combination of values for mobility and carrier density in donor-doped crystals that are often considered mutually exclusive. This combination enables high-quality factor plasmons in the mid-infrared. In addition, a comprehensive and self-consistent model explaining the electrical, optical and thermal properties of CdO is introduced.

CMOs are an ideal class of materials for lower-energy plasmonics as they do not exhibit interband transitions in the mid-infrared. The optical properties can be described using a lossy Drude electron plasma model with a complex dielectric function[12–16]

$$\varepsilon = \varepsilon_1 + i\varepsilon_2 = \varepsilon_\infty - \frac{\omega_p^2}{\omega(\omega + i\gamma)}$$

Here, $\varepsilon_1 + i\varepsilon_2$ is the dielectric function, $\varepsilon_\infty$ is the high-frequency limit of permittivity, $\omega_p$ is the plasma frequency (proportional to the free-carrier concentration) and $\gamma$ is the damping factor describing the scattering and ohmic losses (Supplementary Information). When mobility increases, losses ($\varepsilon_2$) are reduced, and the model predicts enhanced plasmonic performance. Following this relationship, one recognizes immediately the need for a

[1]Department of Materials Science, North Carolina State University, Raleigh, North Carolina 27695, USA. [2]Department of Mechanical Engineering and Materials Science and Department of Electrical Engineering, Duke University, Durham, North Carolina 27708, USA. [3]Department of Materials Science and Engineering, University of Virginia, Charlottesville, Virginia 22904, USA. [4]Department of Mechanical and Aerospace Engineering, University of Virginia, Charlottesville, Virginia 22904, USA. [5]Sandia National Laboratories, Albuquerque, New Mexico 87185, USA. [6]Department of Chemistry, North Carolina State University, Raleigh, North Carolina 27695, USA. *e-mail: stefano.curtarolo@duke.edu; jpmaria@ncsu.edu

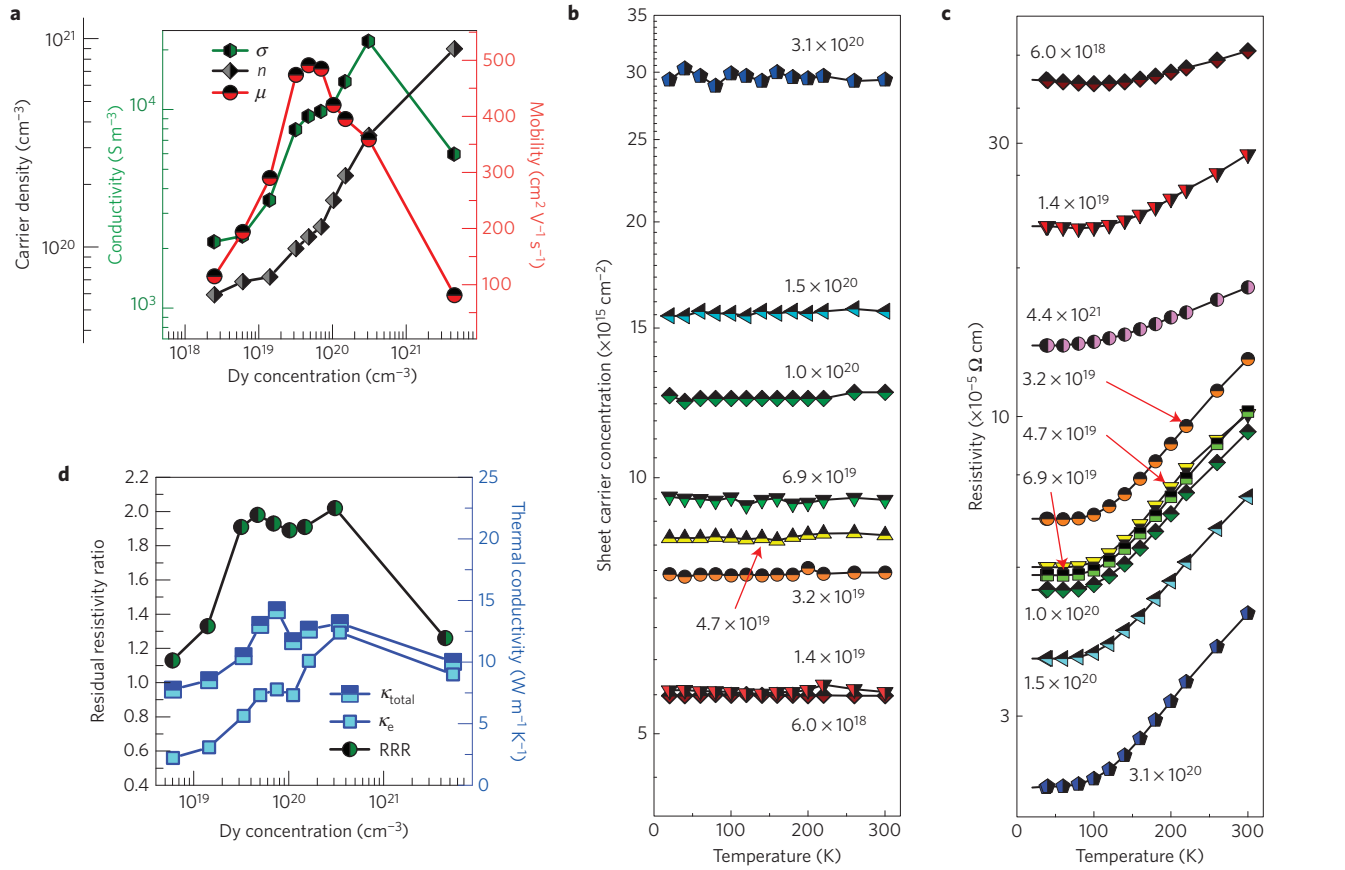


**Figure 1 | Doping- and temperature-dependent properties of CdO:Dy. a**, Transport data for CdO:Dy grown on MgO(100) substrates summarizing carrier concentration (cm$^{-3}$), carrier mobility ($\mu$) and conductivity ($\sigma$) as a function of dysprosium concentration. **b**, Temperature-dependent sheet carrier concentration ($n_s$) as a function of [Dy] for CdO:Dy grown on MgO(100) substrates. **c**, Temperature-dependent resistivity (Ω cm) as a function of [Dy] grown on MgO(100) substrates. **d**, Residual resistivity ratio, measured thermal conductivity ($\kappa_t$) and theoretical values for the electron contribution to thermal conductivity ($\kappa_e$) calculated using the Wiedemann–Franz law for CdO:Dy grown on MgO(100) substrates as a function of Dy concentration.

high-mobility material at carrier concentrations that establish plasma frequencies in the mid-infrared ($n_e > 10^{20}$ cm$^{-3}$), which is a recognized challenge for conventional semiconductors.

In 1969, it was shown that combinations of mobility and carrier density approaching the needs of mid-infrared plasmonics can be achieved in intrinsic CdO single crystals[17]. Vacant oxygen sites, the preferred native defect in CdO, were the source of carriers and were modulated by reducing anneals. However, precise and reproducible control of electrical transport by reduction is a challenge, particularly considering the proximity in temperature and pressure to conditions that destabilize the entire crystal. It is thus reasonable to expect that doping with the correct aliovalent cation may enable further optimization. To explore this hypothesis, we developed a plasma-assisted molecular-beam epitaxy method to synthesize Dy-doped CdO. In a CdO host, Dy populates the Cd sublattice with a 3$^+$ charge, and thus acts as an electron donor. The initial experiment produced four dopant series of epitaxial layers, each on a different substrate, thus offering a range of orientation and mismatch possibilities.

Room-temperature transport properties for a doping series of CdO:Dy grown on MgO(100) substrates are shown in Fig. 1a. Two trends are of particular interest. First, the free-electron concentration is directly proportional to the dysprosium content, and an n-type doping range spanning $5 \times 10^{19}$–$1 \times 10^{21}$ cm$^{-3}$ is accessible. Second, the free-carrier mobility increases with Dy doping, reaching a maximum of almost 500 cm$^2$ V$^{-1}$ s$^{-1}$ at $5 \times 10^{19}$ cm$^{-3}$. After this point, mobility falls steadily until the solubility limit is reached at $5 \times 10^{21}$ cm$^{-3}$. This mobility dependence was observed qualitatively on three additional substrates (MgO(111), GaN(002) and $Al_2O_3$ (006)—see Supplementary Figs 1–3), and in each case the same 3–5 times increase in mobility was found. X-ray diffraction analysis of CdO(002) rocking curves shows no dependence on Dy content until phase separation (see Supplementary Figs 4 and 5). Consequently, crystalline disorder cannot explain this unusual mobility trend.

To understand this dependency, we consider the defect equilibria within the CdO–Dy system as described by the intrinsic and extrinsic defect reactions:

$$Cd_{Cd}^{\ x} + O_O^{\ x} \Longleftrightarrow Cd_{Cd}^{\ x} + V_O^{\ \cdot\cdot} + 2n + \frac{1}{2}O_2(g) \quad (1)$$

$$Dy_2O_3 \xrightarrow{CdO} 2Dy_{Cd}^{\ \cdot} + 2O_O^{\ x} + 2n + \frac{1}{2}O_2(g) \quad (2)$$

CdO is an intrinsic n-type semiconductor, in which electrons originate from doubly ionized O vacancies (equation (1)). The carrier density depends on the ratio of the O-vacancy formation energy to $k_BT$. Aliovalent cations, such as Dy, populate the Cd sublattice and act as extrinsic donors (equation (2)). The interplay between the two reactions and their cooperative equilibration is the key to understanding the present mobility trend. Dy doping pins the extrinsic electron concentration ($n_e$) in proportion to its molar fraction. This is established by flux ratios during growth. The intrinsic reaction is now forced to equilibrate in the presence of a potentially large $n_e$. By Le Chatelier's principle, the intrinsic defect reaction will be driven to the reactant side, which in turn lowers the concentration of O vacancies.

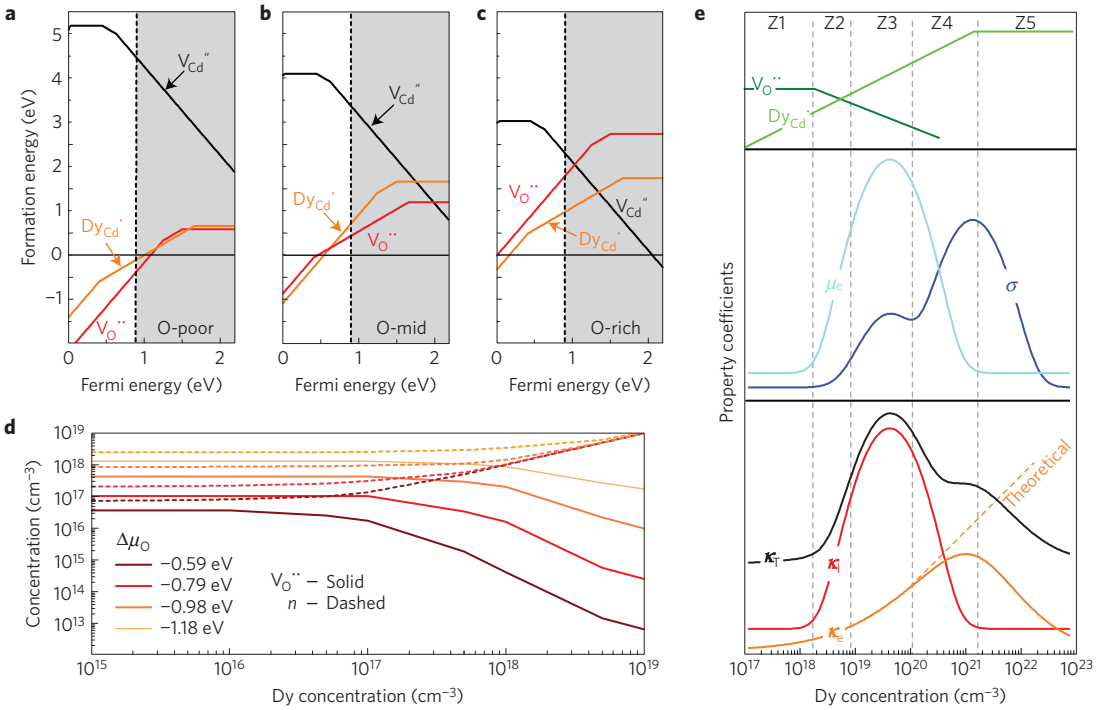


**Figure 2 | DFT calculations and mechanistic zone model for lattice defects in CdO:Dy. a–c**, Defect formation energies as a function of Fermi level for oxygen vacancies ($V_O^{\cdot\cdot}$), cadmium vacancies ($V_{Cd}''$), and Dy substituents on the Cd site ($Dy_{Cd}^{\cdot}$) in the O-poor (**a**), O-mid (**b**) and O-rich (**c**) limits. The slope of each line at a given Fermi level corresponds to the charge of the defect at that Fermi level. **d**, $V_O^{\cdot\cdot}$ concentration (solid lines) and carrier concentration $n$ (dashed lines) as a function of $Dy_{Cd}^{\cdot}$ concentration. Plots are shown for a set of given oxygen chemical potentials, reported as $\Delta\mu_O$ relative to the O-rich extreme with more negative values being more O-poor. **e**, Idealized schematic summarizing the individual contributions of defects to the observed electronic transport in CdO:Dy. [$V_O^{\cdot\cdot}$], [$Dy_{Cd}^{\cdot}$], mobility ($\mu_e$) and conductivity ($\sigma$) are plotted versus [Dy]. Lattice thermal conductivity ($\kappa_l$), total thermal conductivity ($\kappa_t$), electronic thermal conductivity ($\kappa_e$) and the theoretical values for $\kappa_e$ are also plotted versus [Dy]. The Dy-doping space is divided into 5 different zones, where within each zone the observed transport is regulated by a different mechanism.

Dysprosium on a Cd site and an oxygen vacancy are both electron donors. However, as Dy and Cd have similar ionic radii ($r_{Cd^{2+}} = 0.95$ nm; $r_{Dy^{3+}} = 0.92$ nm (ref. 18)), we expect that their substitution will perturb the CdO lattice less than an oxygen vacancy. Consequently, Dy doping creates carriers while reducing the concentration of vacant O sites and the net lattice strain from point defects falls. Furthermore, the primary donor is now a singly positively charged cation, as opposed to a doubly positively charged vacancy. As the impurity scattering potential scales with $Z^2$, at the same carrier density, there is less net scattering for $2n$ donors of charge $e$ than for $n$ donors of charge $2e$ (ref. 19). Both effects will reduce carrier scattering and thus increase mobility.

This model has implications regarding additional properties, amongst them are low-temperature resistivity and room-temperature thermal conductivity, which must share parallel dependencies on Dy content. Figure 1b,c depicts the temperature-dependent sheet carrier concentration, $n_s$, and resistivity, and leads to three observations: $n_s$ is temperature independent, the temperature coefficient of resistivity is positive, and the residual resistivity ratio (RRR, $\rho_{300K}/\rho_{20K}$) increases with Dy doping. Overall, the data imply that CdO:Dy behaves as a metal and that mobility is inversely proportional to temperature; the doping level of $\sim 5 \times 10^{19}$ cm$^{-3}$ exhibits the highest mobility; and that adding impurity cations reduces the number of lattice defects, and/or the extent to which these scatter electrons.

To disentangle the phenomena, thermal conductivity was measured for this film series using the thermoreflectance technique[20]. Total thermal conductivity ($\kappa_t$), and the electronic component of thermal conductivity ($\kappa_e$) are superimposed with the RRR data in Fig. 1d. Both $\kappa_t$ and RRR exhibit two maxima. The first corresponds to the [Dy] producing maximum mobility, and the second lies at a concentration approximately 10 times higher (more details later). As a final observation, all measured properties and trends degrade for the highest Dy concentration ($4 \times 10^{21}$ cm$^{-3}$), which approaches the Dy-solubility limit.

The equilibrium of defects was characterized with density functional theory (DFT) calculations to extract formation energies (at different charge states), for oxygen and cadmium vacancies ($V_O$, $V_{Cd}$), and dysprosium substituents (on the Cd site—$Dy_{Cd}$; ref. 21). As an example, equation (2) expresses the formation energy for Dy substituted on a Cd site:

$$E_f|Dy_{Cd}^q| = E_{DFT}|Dy_{Cd}^q| - E_{DFT}|Bulk| + \mu_{Cd} - \mu_{Dy} + qE_F + E_{Corr}$$

Here, $E_{DFT}|Dy_{Cd}^q|$ is the total DFT energy of Dy on a Cd site in CdO in charge state $q$, and $E_{DFT}|Bulk|$ is the total DFT energy of the perfect bulk structure. The defect formation energies depend on the Fermi level, $E_F$, as well as the O, Cd and Dy chemical potentials ($\mu_O$, $\mu_{Cd}$ and $\mu_{Dy}$). This approach enables a particularly useful representation where defect formation energies are plotted versus $E_F$, as shown in Fig. 2a–c. Fermi energies are referenced to the valence band maximum.

The vertical dotted line at ~0.9 eV represents the conduction band minimum, and the grey region corresponds to the energy range between the indirect and direct bandgaps. The slope for each formation energy curve indicates the most energetically favourable charge state for a given $E_F$. For instance, $Dy_{Cd}$ transitions from a doubly ionized ($Dy_{Cd}^{\cdot\cdot}$) to a singly ionized ($Dy_{Cd}^{\cdot}$) state in the mid-gap region, whereas $V_O$ prefers a +2 charge state ($V_O^{\cdot\cdot}$) across the entire indirect bandgap. At the O-poor limit, there is a substantial energy window where defect formation energies are negative, indicating CdO instability as a host.

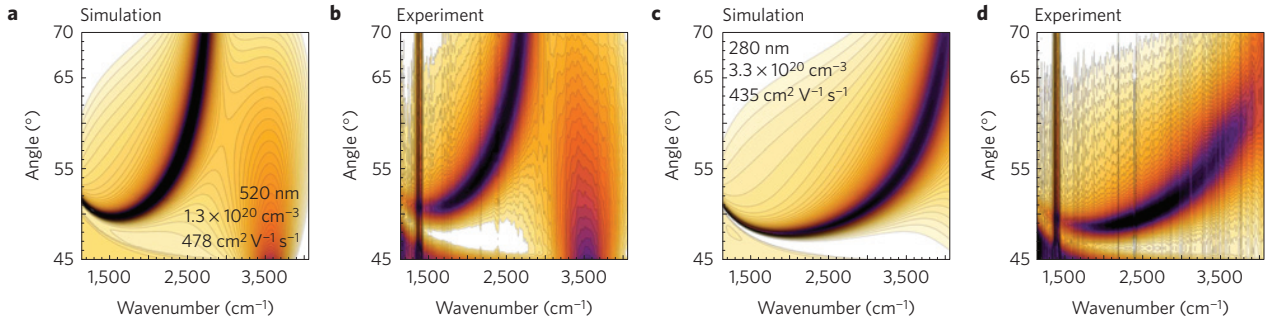


**Figure 3 | Reflectivity maps for CdO:Dy thin films recorded in the Kretschmann configuration. a–d**, Simulated reflectivity data using the tabulated properties as input (**a**,**c**), and experimental data (**b**,**d**) for CdO:Dy with $1.3\times10^{20}$ (**a**,**b**) and $3.3\times10^{20}$ cm$^{-3}$ (**c**,**d**). In each map, the SPP dispersion can be seen as an angle-dependent dip in the reflected light intensity (darker shades). The tunability of the SPP with changing carrier concentration can be seen as the shift of the reflectance dips towards higher energies. The high carrier mobility in CdO:Dy (low loss) results in the sharp absorption bands seen both in experimental and simulated data.

Considering the high activity of atomic oxygen and that CdO is prepared under an oxygen plasma, it is sensible to assume defect equilibration under modest oxygen potentials (that is, between the O-rich and O-mid scenarios of Fig. 2a–c). Then, the implications are: formation energies for $V_{Cd}$ are generally large and metal vacancies are unlikely to be the prevalent defect; for all $E_F > E_g/2$ (the range of interest for n-type materials), the formation energy for $Dy_{Cd}$ is less than that for $V_O$; and $Dy_{Cd}$ and $V_O$ both increase $E_F$ owing to their donor behaviour, and thus their formation energies increase with their concentration. As oxygen vacancies prefer double ionization, their formation energies increase twice faster than $Dy_{Cd}$. Consequently, doping with Dy to concentrations driving $E_F$ to the conduction band minimum would increase the cost of electronically compensated oxygen vacancies by more than 1 eV, markedly reducing their concentrations.

The CdO:Dy defect equilibrium can be calculated by self-consistently solving the mass balance equations[22]. Figure 2d shows $[V_O^{\cdot\cdot}]$ and $n$ versus $[Dy_{Cd}^{\cdot}]$ for the pertinent range of $\mu_O$ keeping $E_F$ within the indirect bandgap. We restrict $E_F$ to this range because the solver uses an effective density of states approximation—valid only for non-degenerate semiconductors. The solver predicts a reduction in $V_O$ and an increase in $n$ as $[Dy_{Cd}^{\cdot}]$ exceeds the equilibrium $[V_O^{\cdot\cdot}]$ for undoped CdO. Although quantitative prediction is limited with respect to $E_F$ (and thus carrier concentration), the trends are expected to persist in degenerate crystals considering that the Fermi level will continue to increase through the Moss–Burstein[23,24] effect (conduction band filling).

The radial strains up to the third-nearest neighbours for $V_O^{\cdot\cdot}$ and $Dy_{Cd}^{\cdot}$ were calculated by DFT to connect the reduction in $[V_O^{\cdot\cdot}]$ with the implied reduction in scattering and an increase in mobility. The results are reported in Table 1. $V_O^{\cdot\cdot}$ introduces approximately twice the radial strain on its nearest neighbours as $Dy_{Cd}^{\cdot}$. Consequently, replacing oxygen vacancies with Dy as the predominant electron donor will reduce the electron and phonon scattering through reduced lattice distortion. As a premium, reducing the formal charge of the majority defect (replacing $V_O^{\cdot\cdot}$ with $Dy_{Cd}^{\cdot}$) will reduce the impurity scattering potential, and thus increase electron mobility. An alternative explanation is that $[V_O]$ remains constant, but association with $Dy_{Cd}$ (existing in the opposite strain state) will relax the overall strain. Additional calculations showed that defect clustering was energetically unfavourable. This is reasonable: the mechanical strain relaxed by complex formation cannot overcome Coulombic repulsion between $V_O^{\cdot\cdot}$ and $Dy_{Cd}^{\cdot}$.

One can now explain the trends observed in Fig. 1a by considering how the population of each defect type depends on Dy, and how the changing populations of each will influence transport. The expected behaviour is illustrated in Fig. 2e.

**Table 1 | Calculated radial strains in CdO due to oxygen vacancies and dysprosium on cadmium sites.**

| NN | #NN | $\varepsilon$ ($V_O^{\cdot\cdot}$) | $\varepsilon$ ($Dy_{Cd}^{\cdot}$) |
|---|---|---|---|
| 1 | 6 | 0.041 | −0.023 |
| 2 | 12 | −0.023 | 0.011 |
| 3 | 8 | 0.004 | −0.001 |

NN, defining the first, second and third sphere of nearest neighbours in CdO; #NN, the number of nearest neighbours in the respective sphere.

Oxygen vacancies ($V_O^{\cdot\cdot}$), lattice thermal conductivity ($\kappa_l$), electronic thermal conductivity ($\kappa_e$) and mobility ($\mu_e$) are represented by green, red, orange and cyan lines, respectively. Conductivity ($\sigma$) is plotted in blue, total thermal conductivity ($\kappa_{total}$) in black, and theoretical values for $\kappa_e$ (from Wiedemann–Franz law) are plotted as an orange dashed line ($\kappa_{e,theory}$). We split [Dy] space into five zones, each exhibiting a different mechanism to regulate transport.

In zone 1, the population of oxygen vacancies—the majority defect—greatly exceeds $[Dy_{Cd}^{\cdot}]$ and the material behaves as an n-type semiconductor.

In zone 2, conduction electrons from extrinsic Dy donors exceed the native value, and $E_F$ consequently increases. The formation energy for $V_O^{\cdot\cdot}$ increases, $[V_O^{\cdot\cdot}]$ falls sharply, and the overall radial strain falls. This leads to increased free-carrier mobility and decreased phonon scattering. The conductivities rise accordingly.

In zone 3, electron and phonon transport reach a broad maximum. The maximum occurs because there is a diminishing reduction in overall strain and the replacement of doubly charged oxygen vacancy donors with singly charged Dy donors as the crystal lattice gets populated with additional $Dy_{Cd}^{\cdot}$. Reduced scattering in this zone is responsible for the first maxima in RRR and $k_{total}$ in Fig. 1d. At the higher end of this doping zone, the strain caused by additional $Dy_{Cd}^{\cdot}$ can no longer be compensated with a further reduction in $V_O^{\cdot\cdot}$. As a result, we observe a reduction in $\kappa_l$ and $\mu_e$ with $Dy_{Cd}^{\cdot}$ concentrations exceeding $5\times10^{19}$ cm$^{-3}$.

In zone 4, strain, and therefore scattering, from $Dy_{Cd}$ continues to increase. However, the observed properties are now governed by the steadily increasing number of free carriers. Electrical and thermal conductivity both increase to a second maximum wherein the amount of conduction electrons compensates for the decreasing carrier and phonon mobilities. As indicated by the theoretical curve ($\kappa_{e,theory}$), the electronic contribution to thermal conduction becomes increasingly important with rising $Dy_{Cd}^{\cdot}$ levels. The observed rise in RRR, $\kappa_{total}$ and $\sigma$ results from a steadily increasing free-carrier concentration.

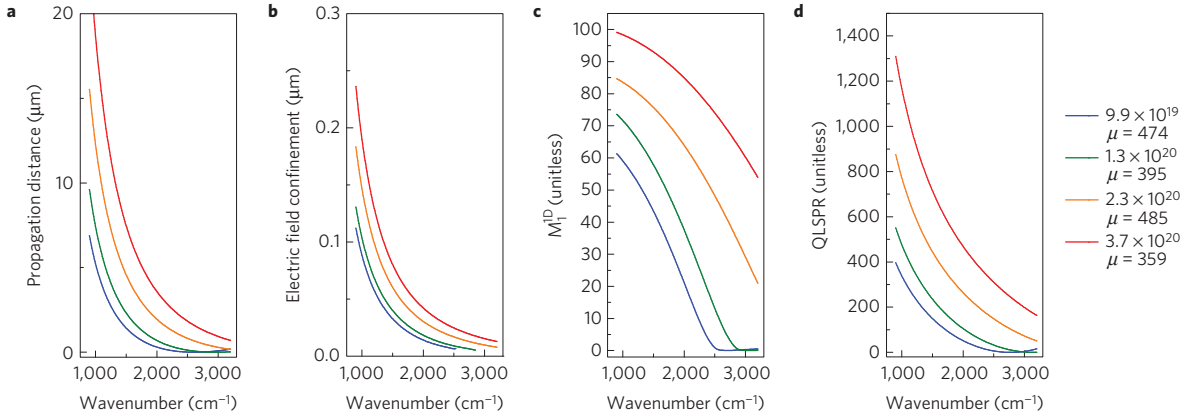


**Figure 4 | Calculated quality factors for four selected CdO:Dy alloys as a function of energy. a**, Calculated SPP propagation distances. **b**, Calculated electric field confinement for the SPP. **c**, Calculated $M_1^{1D}$ figures of merit. **d**, Calculated QLSPR figures of merit. The values of the dysprosium concentrations of the different alloys and the corresponding carrier mobility $\mu$ is shown in the legend.

In zone 5, the solubility limit of Dy in CdO is reached and Dy precipitation starts. Transport properties decrease as insulating secondary phases nucleate between highly disordered grain boundaries. The transport property trends deviate sharply from the classical semiconductor model.

The unique combination of high carrier density and high mobility makes CdO:Dy an ideal plasmonic host at mid-infrared frequencies. Dielectric functions of CdO:Dy indicate that losses are low and that the plasma frequency $\omega_p$ is tunable through the entire mid-infrared range (see Supplementary Fig. 6). To demonstrate experimentally the utility of CdO:Dy for plasmonic devices, epitaxial films were prepared on a MgO(100) substrate with Dy concentrations supporting surface plasmon polaritons (SPPs) that can be excited optically using an IR-Ellipsometer in the Kretschmann–Rather configuration.

To visualize the response, the data are assembled into maps of reflected intensity against incident angle and energy. In such maps, the SPP dispersion is represented by a band of minimum intensity where energy is coupling into the SPP. Figure 3a,c shows reflectivity maps for CdO with $1 \times 10^{20}$ and $3 \times 10^{20}$ carriers $cm^{-3}$ respectively. The shifting reflectivity minimum illustrates how carrier concentration can tune the SPP over the entire mid-infrared range, that is, between 2,500 $cm^{-1}$ and 4,000 $cm^{-1}$. Note that angle-independent (vertical) absorption lines are caused by dark bands in the IR-Ellipsometer's infrared source (see Supplementary Methods). Figure 3b,d shows companion simulations of reflectivity for the same CdO films where CdO optical properties are described by the Drude model. Close agreement is found at all angles and all energies, corroborating our approach and the theoretical treatment of the degenerate semiconductor CdO:Dy as a Drude metal.

Having established the appropriateness of treating CdO as a Drude metal, it is possible to evaluate its plasmonic performance using figures of merit based on propagation distance and field confinement. Such evaluations were demonstrated in a recent report for noble metals, nitrides and conventional transparent conducting oxides[4]. An important conclusion of this (and other) reviews was a paucity of materials offering a combination of carrier density and mobility that yielded an appealing plasmonic response in the near- to mid-infrared spectrum. The carrier density of elemental metals cannot be reduced to sufficiently small densities to access the infrared, whereas the carrier mobilities of traditional CMOs are disappointingly modest.

Figure 4a,b shows the propagation distance and electric field confinement width for SPPs on CdO:Dy in air as a function of wavelength. The quotient of these values, $M_1^{1D}$, is the plasmonic figure of merit that accounts for the inexorable trade-off between propagation distance and field confinement. Gold, which is the standard reference conductor for plasmonic applications, exhibits $M$ values between 10 and 100 over its wavelength region of interest, the visible spectrum. In comparison, the $M$ values for CdO:Dy fall in the exact same range for its spectrum of interest, the near- to mid-infrared. In the case of CdO:Dy, the exceptionally small confinement width is responsible for this attractive performance.

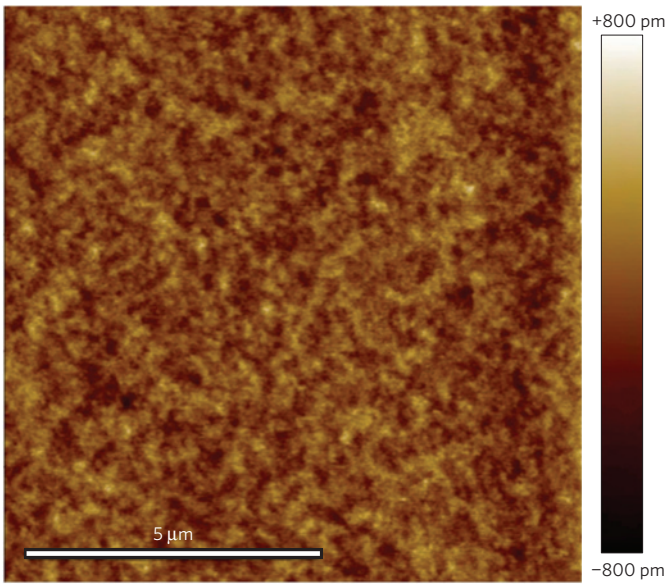


**Figure 5 | Surface quality of CdO:Dy on MgO(100) substrates.** Atomic force microscope topography scan of as-grown CdO:Dy demonstrating the atomically flat growth habit of CdO:Dy on MgO(100) substrates. The observed r.m.s. roughness is <150 pm.

Finally, Fig. 4d shows calculated quality factors for two-dimensional non-spherical CdO waveguides[25] (QLSPR) as a function of energy. The best CdO:Dy alloy presented here exceeds previously published values of nitrides and oxides by a substantial margin, and once again, QLSPR values (in their respective energy ranges) for Au and CdO are comparable. More generically, one can compare the real and imaginary components of the dielectric function in the vicinity of the crossover frequency where $\varepsilon_1 = 0$. Ultimately, a small imaginary component is desirable in this range as it supports a low-loss plasma oscillation. Considering the dielectric data at crossover ensures a self-consistent comparison of materials

with a range of carrier density values. The dielectric properties of CdO:Dy and other materials discussed in this Article are compared in the Supplementary Table 1. In the range $-2 \leq \varepsilon_1 \leq 0$ the imaginary component of CdO:Dy is substantially smaller. Collectively, these metrics quantify CdO:Dy as a high-performance plasmonic material with performance comparable to noble metals in a wavelength range that was previously inaccessible.

Optimal transport and optical properties are not the only attributes necessary for low-loss plasmonics; a contributing factor for any waveguiding application is surface and interface quality. Plasmon propagation distance strongly correlates with surface roughness. A rough surface will change the dispersion relation of SPPs, and increase the loss function owing to the emission of photons[26]. For Ag and Au, atomically flat surfaces are difficult to create. These elements tend to form islands in the thickness range of several nanometres required for optimal mid-infrared interactions[27,28]. Furthermore, the grain size of thin metal films prepared under conditions that dissuade dewetting are typically comparable to film thickness. Consequently, thin noble metal films are populated by numerous grain boundaries and scattering polaritons, reducing the overall plasmonic performance[29,30].

In contrast, when assisted by an oxygen plasma, CdO:Dy can be grown with exceptional surface quality, even with thickness values of 400 nm. Thick films grown on MgO(100) substrates exhibit a root mean squared (r.m.s.) roughness of $<150$ pm ($10\,\mu m^2$ measurement area) that translates to atomically flat surfaces. Figure 5 depicts a $10 \times 10\,\mu m$ atomic force microscopy scan demonstrating the surface quality. Scanning electron microscope images of the same surface (Supplementary Fig. 7) show over wider fields of view that a featureless surface morphology is sustained to thickness values exceeding 400 nm. This remarkable smoothness is attributed to the high-energy O species impacting the substrate during film growth[31].

## Conclusions

In this Article we introduced CdO:Dy as a promising new candidate for studying plasmonic phenomena in the mid-infrared. The ability to understand and engineer coupled lattice defects leads to transport and optical properties that are infrared-relevant and enabling. CdO:Dy can be reliably grown in an oxide molecular beam epitaxy (MBE) environment, and the plasma frequency is tunable over a wide energy range in the mid-infrared. The resulting losses are low owing to very high ($>300\,cm^2\,V^{-1}\,s^{-1}$) carrier mobility over the carrier concentration range of interest, and the surfaces are extremely smooth. This desirable collection of plasmonic properties in CdO:Dy can enable future generations of plasmonic devices operating in the mid-infrared. In general, the results suggest that Fermi level pinning can be used to optimize the transport properties in metal oxide systems and, potentially, other semiconductor materials.

## Methods

CdO was grown in an oxide-MBE system using a custom-built inductively coupled 300 W radiofrequency oxygen plasma gun. Cd was deposited from a metal effusion cell and doping was achieved through evaporation of metallic Dy from a dopant cell. Employed Cd fluxes ranged from 2 to $5 \times 10^{13}$ (at $cm^{-2}\,s^{-2}$) and the Dy flux was varied from $1 \times 10^8$ to $3.5 \times 10^{12}$ (at $cm^{-2}\,s^{-2}$) for the doping series. A typical deposition process involves an O background pressure of $3 \times 10^{-6}$ torr (230 W oxygen plasma), substrate temperatures of 350 °C and an atomic O flux of $1 \times 10^{14}$ (at $cm^{-2}\,s^{-2}$) resulting in an average growth rate of 0.9 nm $min^{-1}$.

Reflectivity data were recorded using a Woollam IR-VASE ellipsometer with a custom-built sample stage in the Kretschmann–Raether configuration. A calcium fluoride ($CaF_2$) prism was used to couple light into the samples, and good optical contact was ensured by applying an index-matching fluid (Cargille Series M 1.720). Reflectivity data were recorded for p- and s-polarized light and are plotted as $R = r_p/r_s$.

Room-temperature transport data were measured with the Van der Pauw technique using an Ecopia HMS-3000 Hall Measurement System.

Temperature-dependent transport measurements were carried out using a custom-built transport probe in a Quantum Design MPMS. Thermal conductivity data were acquired by TDTR measurements, an optical pump–probe experiment that uses a train of ultrashort laser pulses to induce a modulated heating event on the surface of the sample. For these measurements, the surface of the various CdO samples was coated with thin metal films. These act as a transducer to relate the absorbed pump energy to the temporal temperature change on the surface of the sample through the thermoreflectance change monitored in the time domain (see Supplementary Methods for further details).

DFT calculations were performed with the Vienna *Ab initio* Simulation Package (VASP) with a plane-wave basis set, as implemented in VASP 5.3 (refs 32,33) using the hybrid exchange–correlation functional of Heyd, Scuseria and Ernzerhof (HSE06). The defect calculations were based on 64-atom supercells with a $2 \times 2 \times 2$ $k$-point mesh, with a relaxation shell out to the third-nearest neighbour around the defect site. Finite-size interactions for the charged defects were accounted for using the sxdefectalign code by C. Freysoldt. (See Supplementary Methods for further details.)

Although Cd interstitials have been previously considered as sources for carriers, recent theoretical work demonstrates that these are energetically disfavourable[34], and therefore they have not been considered here. The HSE06 hybrid exchange–correlation functional[35,36], including a fraction (0.25) of short-range Hartree–Fock exact exchange, was employed in these calculations. This functional more accurately represents the structural and electronic properties of bulk CdO (ref. 34).

In one limiting condition (the O-rich extreme: the upper limit of $\mu_O$ and the lower limit of $\mu_{Cd}$), $\mu_O$ is referenced to molecular O and $\mu_{Cd}$ is set such that $\mu_{Cd} = \mu_{CdO} - \mu_O$. In the opposite limiting condition (the O-poor extreme, the upper limit of $\mu_{Cd}$ and lower limit of $\mu_O$), $\mu_{Cd}$ is referenced to metallic Cd, and $\mu_O$ is set such that $\mu_O = \mu_{CdO} - \mu_{Cd}$. $\mu_{Dy}$ accounts for the $Dy_2O_3$ solubility-limiting phase. $E_{Corr}$ corrects for finite-size effects of the unit cell and is determined through the method refs 37,38.

Received 13 September 2014; accepted 19 December 2014; published online 16 February 2015

## References


1. Johnson, P. B. & Christy, R. W. Optical constants of the noble metals. *Phys. Rev. B* **6,** 4370–4379 (1972).
2. West, P. R. *et al.* Searching for better plasmonic materials. *Laser Photon. Rev.* **4,** 795–808 (2010).
3. Law, S., Podolskiy, V. & Wasserman, D. Towards nano-scale photonics with micro-scale photons: The opportunities and challenges of mid-infrared plasmonics. *Nanophotonics* **2,** 103–130 (2013).
4. Naik, G. V., Shalaev, V. M. & Boltasseva, A. Alternative plasmonic materials: Beyond gold and silver. *Adv. Mater.* **25,** 3264–3294 (2013).
5. Stanley, R. Plasmonics in the mid-infrared. *Nature Photon.* **6,** 409–411 (2012).
6. Brar, V. W., Jang, M. S., Sherrott, M., Lopez, J. J. & Atwater, H. A. Highly confined tunable mid-infrared plasmonics in graphene nanoresonators. *Nano Lett.* **13,** 2541–2547 (2013).
7. Fang, Z. *et al.* Gated tunability and hybridization of localized plasmons in nanostructured graphene. *ACS Nano* **7,** 2388–2395 (2013).
8. Yan, H. *et al.* Damping pathways of mid-infrared plasmons in graphene nanostructures. *Nature Photon.* **7,** 394–399 (2013).
9. Law, S., Adams, D. C., Taylor, A. M. & Wasserman, D. Mid-infrared designer metals. *Opt. Express* **20,** 12155–12165 (2012).
10. Law, S., Yu, L. & Wasserman, D. Epitaxial growth of engineered metals for mid-infrared plasmonics. *J. Vac. Sci. Technol. B* **31,** 03C121 (2013).
11. Rosenberg, A. *et al.* Flat mid-infrared composite plasmonic materials using lateral doping-patterned semiconductors. *J. Opt.* **16,** 094012 (2014).
12. Mendelsberg, R. J., Garcia, G. & Milliron, D. J. Extracting reliable electronic properties from transmission spectra of indium tin oxide thin films and nanocrystal films by careful application of the Drude theory. *J. Appl. Phys.* **111,** 063515 (2012).
13. Losego, M. D. *et al.* Conductive oxide thin films: Model systems for understanding and controlling surface plasmon resonance. *J. Appl. Phys.* **106,** 024903 (2009).
14. Rhodes, C. *et al.* Surface plasmon resonance in conducting metal oxides. *J. Appl. Phys.* **100,** 054905 (2006).
15. Noginov, M. A. *et al.* Transparent conductive oxides: Plasmonic materials for telecom wavelengths. *Appl. Phys. Lett.* **99,** 021101 (2011).
16. Sachet, E., Losego, M. D., Guske, J., Franzen, S. & Maria, J-P. Mid-infrared surface plasmon resonance in zinc oxide semiconductor thin films. *Appl. Phys. Lett.* **102,** 051114 (2013).
17. Koffyberg, F. P. Carrier concentration in oxygen deficient CdO single crystals. *Phys. Lett. A* **30,** 37–38 (1969).

18. Shannon, R. D. Revised effective ionic radii and systematic studies of interatomic distances in halides and chalcogenides. *Acta Crystallogr. A* **32,** 751–767 (1976).
19. Ridley, B. K. Reconciliation of the Conwell–Weisskopf and Brooks–Herring formulae for charged-impurity scattering in semiconductors: Third-body interference. *J. Phys. C: Solid State Phys.* **10,** 1589–1593 (1977).
20. Cahill, D. G. Analysis of heat flow in layered structures for time-domain thermoreflectance. *Rev. Sci. Instrum.* **75,** 5119–5122 (2004).
21. Van de Walle, C. G. & Neugebauer, J. First-principles calculations for defects and impurities: Applications to III-nitrides. *J. Appl. Phys.* **95,** 3851–3879 (2004).
22. Gaddy, B. E. *et al.* Vacancy compensation and related donor–acceptor pair recombination in bulk AlN. *Appl. Phys. Lett.* **103,** 161901 (2013).
23. Burstein, E. Anomalous optical absorption limit in InSb. *Phys. Rev.* **93,** 632–633 (1954).
24. Moss, T. S. The interpretation of the properties of indium antimonide. *Proc. Phys. Soc. B* **67,** 775–782 (1954).
25. Berini, P. Figures of merit for surface plasmon waveguides. *Opt. Express* **14,** 13030–13042 (2006).
26. Raether, H. *Surface Plasmons on Smooth and Rough Surfaces and on Gratings* (Springer, 1988).
27. Herminjard, S. *et al.* Surface plasmon resonance sensor showing enhanced sensitivity for $CO_2$ detection in the mid-infrared range. *Opt. Express* **17,** 293–303 (2009).
28. Kazmerski, L. L. & Racine, D. M. Growth, environmental, and electrical properties of ultrathin metal films. *J. Appl. Phys.* **46,** 791–795 (2008).
29. Hövel, H., Fritz, S., Hilger, A., Kreibig, U. & Vollmer, M. Width of cluster plasmon resonances: Bulk dielectric functions and chemical interface damping. *Phys. Rev. B* **48,** 18178–18188 (1993).
30. Kraus, W. A. & Schatz, G. C. Plasmon resonance broadening in small metal particles. *J. Chem. Phys.* **79,** 6130–6139 (1983).
31. Sohn, M. H., Kim, D., Kim, S. J., Paik, N. W. & Gupta, S. Super-smooth indium–tin oxide thin films by negative sputter ion beam technology. *J. Vac. Sci. Technol. A* **21,** 1347–1350 (2003).
32. Kresse, G. & Hafner, J. *Ab initio* molecular dynamics for liquid metals. *Phys. Rev. B* **47,** 558–561 (1993).
33. Kresse, G. & Hafner, J. *Ab initio* molecular-dynamics simulation of the liquid-metal–amorphous-semiconductor transition in germanium. *Phys. Rev. B* **49,** 14251–14269 (1994).
34. Burbano, M., Scanlon, D. O. & Watson, G. W. Sources of conductivity and doping limits in CdO from hybrid density functional theory. *J. Am. Chem. Soc.* **133,** 15065–15072 (2011).
35. Heyd, J., Scuseria, G. E. & Ernzerhof, M. Hybrid functionals based on a screened Coulomb potential. *J. Chem. Phys.* **118,** 8207–8215 (2003).
36. Heyd, J., Scuseria, G. E. & Ernzerhof, M. Hybrid functionals based on a screened Coulomb potential. *J. Chem. Phys.* **118,** 8207 (2003); erratum **124,** 219906 (2006).
37. Freysoldt, C., Neugebauer, J. & Van de Walle, C. G. Fully *ab initio* finite-size corrections for charged-defect supercell calculations. *Phys. Rev. Lett.* **102,** 016402 (2009).
38. Freysoldt, C., Neugebauer, J. & Van de Walle, C. G. Electrostatic interactions between charged defects in supercells. *Phys. Status Solidi B* **248,** 1067–1076 (2011).


## Acknowledgements

S.F. and J-P.M. gratefully acknowledge support of this work by NSF grant CHE-1112017. The NSF grant DMR-1151568 supported the DFT contributions. We would further like to acknowledge Efimenko and Genzer (NCSU, CBE) for granting us access to the IR-Ellipsometer. Sandia National Laboratories is a multi-programme laboratory managed and operated by Sandia Corporation, a wholly owned subsidiary of Lockheed Martin Corporation, for the US Department of Energy's National Nuclear Security Administration under contract DE-AC04-94AL85000. The thermal conductivity measurements were supported by the Air Force Office of Scientific Research under AFOSR Award No. FA9550-14-1-0067 (Subaward No. 5010-UV-AFOSR-0067) and the ONR Young Investigator Program (N00014-13-4-0528). S.C. acknowledges the Duke Center for Materials Genomics and partial support by ONR (MURI N00014-13-1-0635).

## Author contributions

E.S., S.F. and J-P.M. proposed the concept and experiments with support by S.C. C.T.S. and E.S. developed the MBE deposition and doping technique for the growth of CdO:Dy. E.S. led the experimental/analytical efforts with support from C.T.S., B.F.D., P.E.H., P.A.S., A.L.S. and J.I. The DFT simulations and analysis of theoretical results were performed by D.L.I., B.E.G. and J.S.H. All authors mentioned above discussed and contributed to the paper.

## Additional information

Supplementary information is available in the online version of the paper. Reprints and permissions information is available online at www.nature.com/reprints. Correspondence and requests for materials should be addressed to S.C. or J-P.M.

## Competing financial interests

The authors declare no competing financial interests.